Two-Steps Halogen Intercalation Mechanism in Dual-Ion Batteries Enabled by Aqueous Biphasic Systems

Damien Degoulange[1,2,3], Gwenaëlle Rousse[1,2,3], Alexis Grimaud[1,2,3,4*]

1. Chimie du Solide et de l'Energie, UMR 8260, Collège de France, 75005 Paris, France

2. Sorbonne Université, 4 place Jussieu, 75005 Paris, France

3. Réseau sur le Stockage Electrochimique de l'Energie (RS2E), CNRS FR3459, 80000 Amiens, France

4. Department of Chemistry, Merkert Chemistry Center, Boston College, Chestnut Hill, MA 02467, USA

***Corresponding author:** Alexis Grimaud (alexis.grimaud@bc.edu)

Abstract

The electrification of our society requires safer and longer lasting batteries, for which modular electrolytes such as aqueous biphasic systems (ABS) are being developed. ABS, *i.e.* two-phase systems, were shown to enable high-potential dual-ion aqueous batteries based on Li-ion (de)intercalation at graphite negative electrode and halides (de)intercalation at graphite positive electrode. However, the exact role of ABS in promoting the intercalation of halogens while preventing halogen gas evolution remains unclear. We find that using ABS do not favor halogen intercalation but rather trihalides formation. Electrochemically-generated trihalides are confined in the halide-rich phase of ABS, preventing their diffusion to negative electrode and self-discharge. We also revealed that confined trihalides spontaneously intercalate in the graphite positive electrode. ABS thus enable a two-steps electrochemical-chemical intercalation mechanism of halogens. This work paves the way toward the design of novel ABS for developing dual-ion batteries or membrane-less redox-flow batteries with independent anodic and cathodic chemistries.

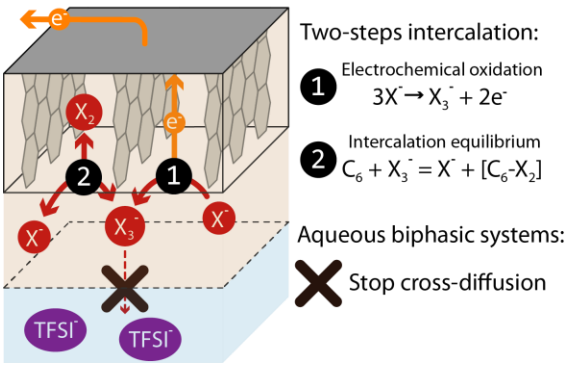

Main text

Li-ion batteries have conquered the market of applications below 100 kWh, from portable devices to electric vehicles.[1] However, to answer the necessary transition from fossil fuels to renewable energy, a massive electrification of our society is ongoing, for which batteries of several GWh will be needed for grid scale applications.[2,3] When reaching such scale, burdens regarding safety and scalability become overriding, creating a regain of interest for aqueous batteries.[4] To combat the limited electrochemical operating window of aqueous electrolytes, new strategies have emerged, among which water-in-salt electrolytes (WiSE), *i.e.* highly concentrated electrolytes where salt outnumbers both in mass and weight the water molecules, quickly became the center of attention.[5] Indeed, highly concentrated environments result in diminished kinetics for oxygen evolution reaction (OER), and formation of a passivation layer preventing hydrogen evolution reaction (HER), both enabling electrochemical stability window of WiSE ≈ 3 V.[6–8]

In pursue of optimal compositions, WiSE using different combinations of salts were tested. Notably, when mixing at high concentration lithium bis(trifluoromethane)sulfonimide (LiTFSI) with smaller, more hydrophilic lithium halide salts such as LiCl or LiBr, aqueous biphasic systems (ABS) were obtained.[9–11] Beside their interest for separation or recycling, ABS in which two immiscible aqueous phases are formed, one phase being TFSI-rich and the other phase being halide-rich, quickly showed interest for battery application as they enable having distinct aqueous electrolytes and thus distinct chemistries at the positive and at the negative electrodes. These chemistries are enabled by the formation of a liquid/liquid interface which is selective for

dissolved ionic species, thus preventing cross-talking events in dual-ion, Li-S or redox flow batteries.[12–15] Especially, an ABS based on LiTFSI, LiCl and LiBr was used in a dual ions battery to enable the reversible intercalation of lithium cations from the LiTFSI-rich solution at the negative electrode and the reversible conversion/intercalation of halide anions from the LiBr/LiCl-rich solution into graphite at the positive electrode[13] (Fig. 1a). This halide conversion/intercalation enables a transition metal-free aqueous battery with a reversible capacity of 243 $mAh.g^{-1}$, for > 200 cycles with 80% capacity retention at 200 $mA.g^{-1}_{graphite}$.

Halogens conversion/intercalation into graphite was reported to occur at high potentials, following two sequential reactions (eq. 1): first bromide is intercalated at 3.95 V vs. Li^+/Li to form $C_6[Br_2]$ followed by chloride intercalation at 4.25 V vs. Li^+/Li to form $C_6[BrCl]$ (Fig. 1b). Both reactions are associated with the oxidation of halide anions, but differ from direct halides oxidation into either halogen gases (eq. 2) or soluble polyhalides (eq. 3).

$$2X^- + C_6 = [C_6 - X_2] + 2e^- \quad (X = Br, Cl) \qquad eq.\ 1$$

$$2X^- = X_{2(g)} + 2e^- \quad (X = Br, Cl) \qquad eq.\ 2$$

$$3X^- = {X_3}^- + 2e^- \quad (X = Br, Cl) \qquad eq.\ 3$$

While X-ray diffraction and X-ray absorption measurements have revealed this conversion/intercalation of halides into graphite[13], the exact role played by the ABS in enabling the intercalation of halogens while preventing competing oxidative reactions remains elusive. More precisely, past studies have revealed effects of high salt concentrations[6,7,16] on redox potentials for reactions involving cations such as Li^+, H^+ or Zn^{2+}, but our current understanding of concentration-dependence of anions redox is still limited.[17–19] Furthermore, ABS are known for

their ability to partition ions, more precisely anions, as previously demonstrated for TFSI[9–11,13,16] or for soluble polysulfides[12]. Nevertheless, very little is known regarding solvation properties and speciation of halide anions in ABS. Developing further multiphasic (ABS) electrolytes for dual-ion or beyond Li-ion battery technologies thus relies on gaining a deeper understanding of the role played by ABS. Hence, we studied the effect of ABS high salt concentrations and liquid/liquid interface in i) modulating redox potentials for halide oxidation and ii) changing the chemical nature and solvation properties of soluble halides in each aqueous phase.

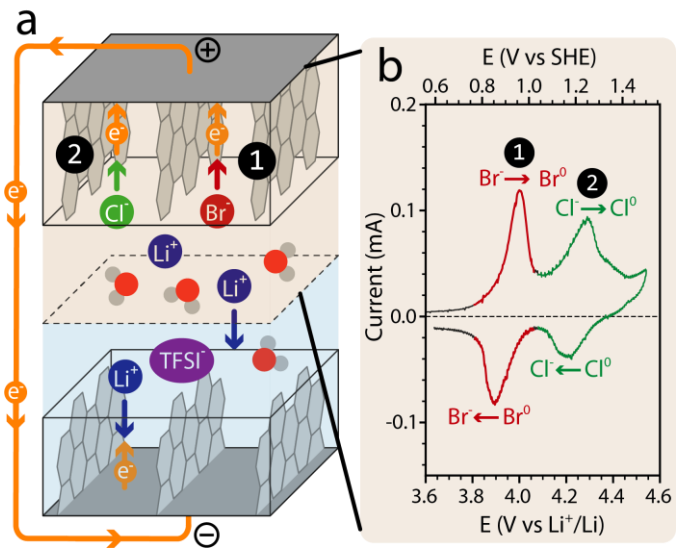

Figure 1. Schematics and cyclic voltammogram of the aqueous battery using ABS forming at high concentration. a, Schematics of the dual ion battery based on halogen conversion/intercalation at the positive electrode and Li-ion intercalation at the negative electrode, using an ABS as electrolyte having a TFSI-rich phase in contact with the negative electrode and a halide-rich phase in contact with the positive electrode. **b**, Three-electrodes cycling voltammetry recorded for the intercalation of halides into graphite, with 1) the intercalation of bromide (red) and 2) the intercalation of chloride (green).

The main difficulty in assessing the redox potentials for Br^- oxidation (or Cl^- oxidation, see below) originates from the co-existence of three reactions (eqs. 4, 6, 8), depending on bromide concentrations and pH, following Nernst potentials (eqs. 5, 7, 9):

$$Br_{2(aq)} + 2e^- = 2Br^-{}_{(aq)} \qquad eq.4$$

$$E = E°_{Br_2/Br^-} + \frac{RT}{2F} ln\left(\frac{a\left(Br_{2(aq)}\right)}{a\left(Br^-{}_{(aq)}\right)^2}\right) \qquad eq.5$$

$$Br_3{}^-{}_{(aq)} + 2e^- = 3Br^-{}_{(aq)} \qquad eq.6$$

$$E = E°_{Br_3{}^-/Br^-} + \frac{RT}{2F} ln\left(\frac{a\left(Br_3{}^-{}_{(aq)}\right)}{a\left(Br^-{}_{(aq)}\right)^3}\right) \qquad eq.7$$

$$BrO_3{}^-{}_{(aq)} + 6H^+{}_{(aq)} + 6e^- = Br^-{}_{(aq)} + 3H_2O_{(l)} \qquad eq.8$$

$$E = E°_{BrO_3{}^-/Br^-} + \frac{RT}{6F} ln\left(\frac{a\left(BrO_3{}^-{}_{(aq)}\right).a\left(H^+{}_{(aq)}\right)^6}{a\left(Br^-{}_{(aq)}\right).\ a\left(H_2O_{(l)}\right)^3}\right) \qquad eq.9$$

with $E°$ the standard potentials, R the molar gas constant, T the temperature, F the faraday constant, $a\left(X^-{}_{(aq)}\right)$ the activities of the different ions and $a\left(H_2O_{(l)}\right)$ the water activity (Supplementary discussion 1)[20].

Calculating the Pourbaix diagram (E = f(pH)) for bromide species[21] as function of bromide concentration (See Materials and Methods), a three-dimensional Pourbaix diagram is obtained (Fig. 2a). For pH above 7, bromide oxidation to bromate (BrO_3^-) is thermodynamically favoured at all concentrations. However, for pH below 7, two oxidation products can exist depending on the bromide concentration. At concentrations below 0.1 mol.kg^{-1} (m), bromide is oxidized to bromine (Br_2). Instead, at concentration above 0.1m, bromide is oxidized to tribromide (Br_3^-). As previously demonstrated, highly concentrated aqueous solutions are slightly acidic[22,16], hence oxidation of bromide to tribromide is thermodynamically favoured in conditions pertinent to ABS.

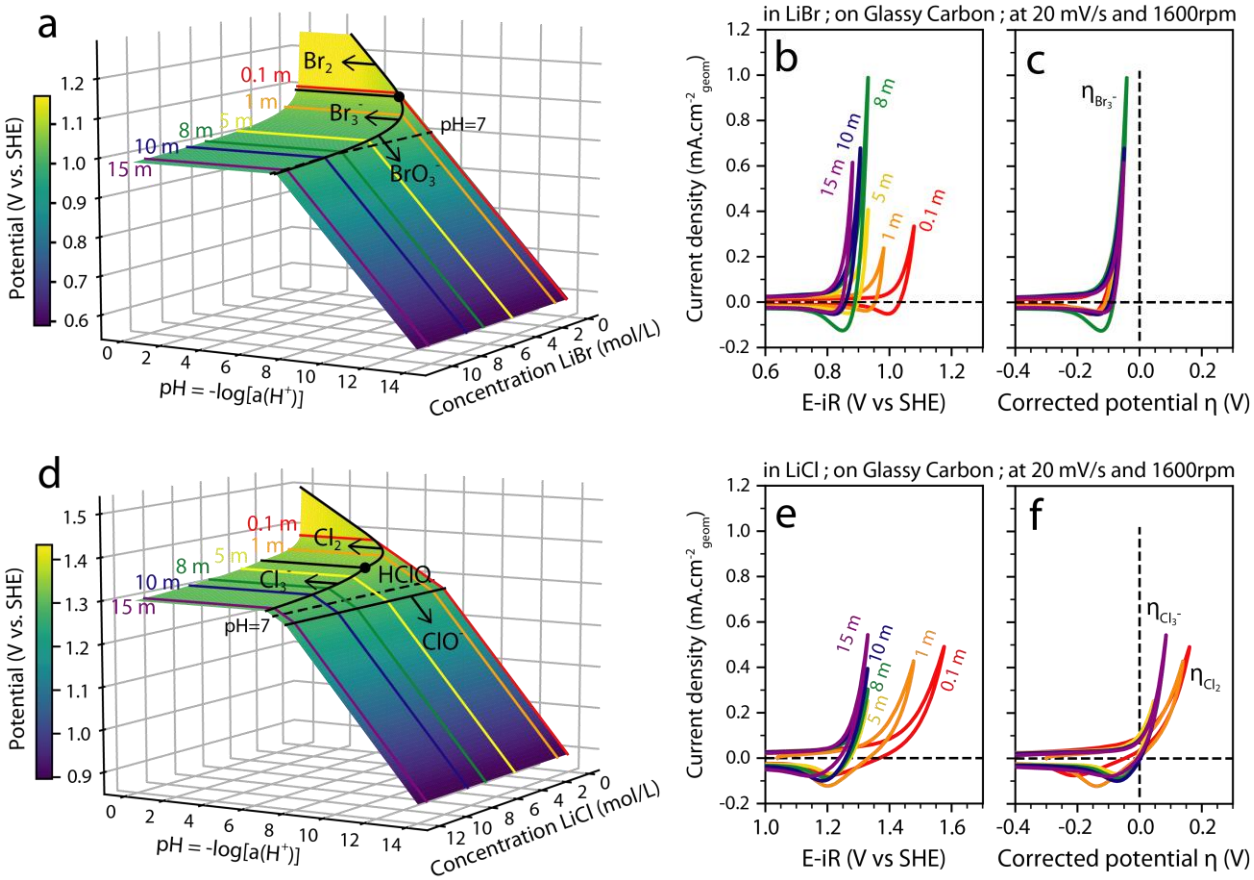

Figure 2. Halogens oxidation in highly concentrated solutions. a, Three-dimensional graph obtained by plotting the Pourbaix diagram of bromide (E = f(pH)) as function of the lithium bromide concentration. **b-c**, Cyclic voltammograms of the bromide oxidation recorded on Glassy Carbon rotating disk electrodes at 1600 rpm for LiBr solutions of concentration between 0.1m and 15m plotted as function of the ohmic drop compensated potential **(b)** or potentials corrected for the oxidation of bromide to tribromide **(c)**. **d**, Three-dimensional graph obtained by plotting the Pourbaix diagram of chloride (E = f(pH)) as function of the lithium chloride concentration. **e-f**, Cyclic voltammograms of the chloride oxidation recorded on Glassy Carbon rotating disk electrodes at 1600 rpm for LiCl solutions of concentration between 0.1m and 15m plotted as function of the ohmic drop compensated potential **(e)** or potentials corrected for the oxidation of chloride to chlorine for concentrations of 0.1m and 1m and corrected for the oxidation of chloride to trichlorine for concentrations between 5m and 15m **(f)**.

Knowing that tribromide is the thermodynamically favored oxidation product at high concentration, a cubic dependence of bromide oxidation potential on LiBr concentration is

expected following eq. 7. Hence, we studied the bromide oxidation by cyclic voltammetry (CV) on glassy carbon rotating disk electrodes (GC-RDE) in electrolytes containing lithium bromide in concentration ranging from 0.1m to 15m (Fig. 2b). Increasing the concentration was found to shift the oxidation toward less positive potentials (Fig. 2b), from 1.05 V vs SHE at 0.1m to 0.85 V vs SHE at 15m. To account for the cubic dependence on bromide concentration of the reversible potential for tribromide formation (eq. 7), potentials were then converted into tribromide corrected potential ($\eta_{Br_3^-}$) (eq. 10, derived from eq. 7) taking into consideration liquid junction potential (LJP) and potential shift due to ions' activity coefficient ($E_{LJP/\gamma}$) (as estimated in Fig. S1)[16]:

$$\eta_{Br_3^-} = E - \left(E^{\circ}{}_{Br_3^-/Br^-} - \frac{RT}{2F} ln\left(c\left(Br^-{}_{(aq)} \right)^3 \right) \right) - iR - E_{LJP/\gamma} \qquad eq.10$$

After conversion, CVs recorded at all concentrations overlap (Fig. 2c), which coincides with bromide oxidation following an inverse cubic dependence on bromide concentration alike what was expected for the tribromide formation. Note that for a reaction with fast kinetics and in the initial absence of the oxidized formed of the redox couple, *i.e.* absence of tribromide in solution (Supplementary discussion 2), negative potentials are expected after correction.[23,24] Comparatively, bromine or bromate formation (eqs. 4-5, 8-9) can be ruled out as, respectively, potentials corrected for a linear or square concentration dependence (eqs. S1-S2) do not overlap (Fig. S2). Hence, we conclude that bromide is oxidized to tribromide at any concentration tested in this study.

The same methodology was applied to the oxidation reactions of chloride (eqs. 11-18). The

theoretical three-dimensional graph obtained by plotting the Pourbaix diagram of the chloride[21] as a function of the chloride concentration is shown in Fig. 2d:

$$Cl_{2\,(aq)} + 2e^- = 2Cl^-{}_{(aq)} \qquad eq.11$$

$$E = E°_{Cl_2/Cl^-} + \frac{RT}{2F} ln\left(\frac{a\left(Cl_{2\,(aq)}\right)}{a\left(Cl^-{}_{(aq)}\right)^2}\right) \qquad eq.\ 12$$

$$Cl_3{}^-{}_{(aq)} + 2e^- = 3Cl^-{}_{(aq)} \qquad eq.13$$

$$E = E°_{Cl_3{}^-/Cl^-} + \frac{RT}{2F} ln\left(\frac{a\left(Cl_3{}^-{}_{(aq)}\right)}{a\left(Cl^-{}_{(aq)}\right)^3}\right) \qquad eq.\ 14$$

$$HClO_{(aq)} + H^+{}_{(aq)} + 2e^- = Cl^-{}_{(aq)} + H_2O_{(l)} \qquad eq.15$$

$$E = E°_{HClO/Cl^-} + \frac{RT}{2F} ln\left(\frac{a\left(HClO_{(aq)}\right).a\left(H^+{}_{(aq)}\right)}{a\left(Cl^-{}_{(aq)}\right).a\left(H_2O_{(l)}\right)}\right) \qquad eq.16$$

$$ClO^-{}_{(aq)} + 2H^+{}_{(aq)} + 2e^- = Cl^-{}_{(aq)} + H_2O_{(l)} \qquad eq.17$$

$$E = E°_{ClO^-/Cl^-} + \frac{RT}{2F} ln\left(\frac{a\left(ClO^-{}_{(aq)}\right).a\left(H^+{}_{(aq)}\right)^2}{a\left(Cl^-{}_{(aq)}\right).a\left(H_2O_{(l)}\right)}\right) \qquad eq.18$$

At pH above 7.5, hypochlorite anions (ClO^-) are formed, while at 6.5 < pH < 7.5, hypochlorous acid (HOCl) is preferentially formed. At lower pH, chloride is oxidized into chlorine (Cl_2) for concentrations below 3m or to trichloride (Cl_3^-) above 3m. Thus, similarly to the bromide

oxidation, the formation of trichloride is expected to be thermodynamically favoured in concentrated solutions that are slightly acidic.[16,22] However, for concentrations of chloride anions below 3m, chlorine or hypochlorous acid formation are expected to be thermodynamically favourable. The experimental CVs recorded as function of LiCl concentration (Fig. 2e) show decreasing oxidation potentials with increasing concentrations, in accordance with Nernst equations (eqs. 12, 14, 16, 18). Plotting the corrected potentials (eqs. S3-S6) for the four chlorine oxidations reactions, none of the corrected potentials overlap at all concentrations (Fig. S3), suggesting that a unique reaction cannot explain the potential shifts in the whole concentration range. Instead, concordant with the three-dimensional Pourbaix diagram, $\eta_{Cl_3^-}$ are found to overlap at concentrations between 15m and 5m, while η_{Cl_2} or η_{HClO} overlap for concentrations ≤ 1m (Fig. 2f). Moreover, the corrected potentials are positive, suggesting an overpotential due to slower kinetics than for the bromide oxidation. Overall, we can conclude that the oxidation of chloride below 3m leads to the formation of chlorine or hypochlorous acid while in regimes pertinent to ABS, *i.e.* above 3m, trichloride is formed. This conclusion is general to halides oxidation, and at high lithium iodide concentration, triiodide is also preferentially formed from the oxidation of iodide (eqs. S7-S12 and Fig. S4).

Our recent studies on ABS show that the halogen-rich (top) phase contains small amount of LITFSI, and vice versa.[9–11] To evaluate the potential impact of LiTFSI and LiCl on bromide oxidation, mix solutions containing both lithium halides (LiBr and LiCl) or LiBr with LiTFSI were studied. Addition of large amount of LiCl (5m to 8m) or small amount (0.1m) of LiTFSI in concentrated LiBr solutions does not lead to substantial changes in bromide oxidation (Fig. S5). Instead, we reveal that by adding large amount (1m to 15m) of LiTFSI in diluted LiBr solutions,

bromide oxidation is facilitated (Fig. S6a) due to potential shift linked to a change in reversible potential and LJP in concentrated LiTFSI solutions (Fig. S1 and Fig. S6b). Hence our results show that a higher salt concentration favors the oxidation of halides to trihalides.

To confirm that trihalides are formed, the equilibrium in concentrated solutions between bromine and tribromide (eq. 19) was assessed:

$$Br_{2(aq)} + Br^{-}{}_{(aq)} = Br_3{}^{-}{}_{(aq)} \qquad eq.19$$

For this, Ultraviolet-Visible (UV-Vis) measurements were carried out for 15m LiBr solution with added bromine (Fig. 3a – in red). The absorption band of Br_3^- (at 277 nm) was solely observed, confirming that tribromide is favorably formed over bromine. Moreover, with the bromine/tribromide equilibrium being displaced toward the formation of tribromide, bromine is found highly soluble in LiBr concentrated solutions, as show in Fig. 3b where a 15m $LiBr_3$ solution was formed by adding equimolar quantities of Br_2 in a 15m LiBr solution. On the contrary, solubility of bromide as estimated from Beer-Lambert law is found limited in 20m LiTFSI (Br_2 solubility in 20m LiTFSI ≈ 0.03 mol.L^{-1} compared to ≈ 0.21 mol.L^{-1} in pure water), and no tribromide was observed as bromide is absent for eq. 19 to take place (Fig. 3a – in orange and Fig. 3c). A table summarizing absorption maxima and absorption coefficient of trihalides and halogens is given in Table S1-S2.[25–29]

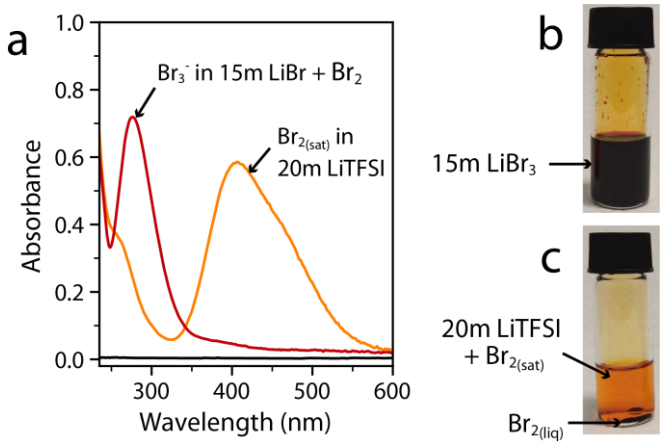

Figure 3. UV-Vis detection and images of Br_3^- and Br_2 in LiBr and LiTFSI, respectively. a, UV-Vis spectra recorded for Br_2 saturated in 20m LiTFSI (orange) and spectra of diluted Br_2 in 15m LiBr forming Br_3^- (red). **b**, Picture of equimolar quantities of Br_2 in 15m LiBr forming a 15m $LiBr_3$ solution. **c**, Picture of the 20m LiTFSI solution saturated in Br_2 (drops of liquid Br_2 are in the solution as it is saturated).

We have demonstrated that monophasic solutions at high concentration such as those encountered in ABS do not prevent halides oxidation, and instead push the oxidation reaction toward the formation of trihalides. Thus, our attention then turned to biphasic systems and understanding the selectivity toward trihalide anions of the liquid/liquid interface formed for the LiTFSi/LiCl-LiBr/H_2O system. For that, Br_3^- was formed in a 10m LiBr - 5m LiTFSI ABS by addition of Br_2. Doing so, we observed the characteristic color and UV-Vis absorption peak associated with tribromide anions only in the halide-rich phase (top phase) (Fig. 4a-b and S7), while the TFSI-rich phase (bottom phase) remains colorless. This finding indicates that tribromide spontaneously separates from the TFSI-rich phase. To confirm this assertion, the phase diagram for the $LiBr_3$-LiTFSI system was determined by cloud point titration and compared with that of LiBr-LiTFSI ABS[9–11] (Fig. 4c). Both phase diagrams are found very similar, with only a slight increase of the miscible domain at large concentration of tribromide along with a slight decrease of the miscible domain

at large concentration of LiTFSI when compared to LiBr. We thus conclude that trihalides behave similarly to halides and thus will not mix into the TFSI-rich phase. This finding has a major implication for the electrochemical device, as trihalides electrochemically generated during battery operation will stay confined in the halide-rich phase at the positive electrode. Hence, the liquid/liquid interface plays a confinement role, avoiding cross-diffusion of the oxidation products toward the negative electrode.

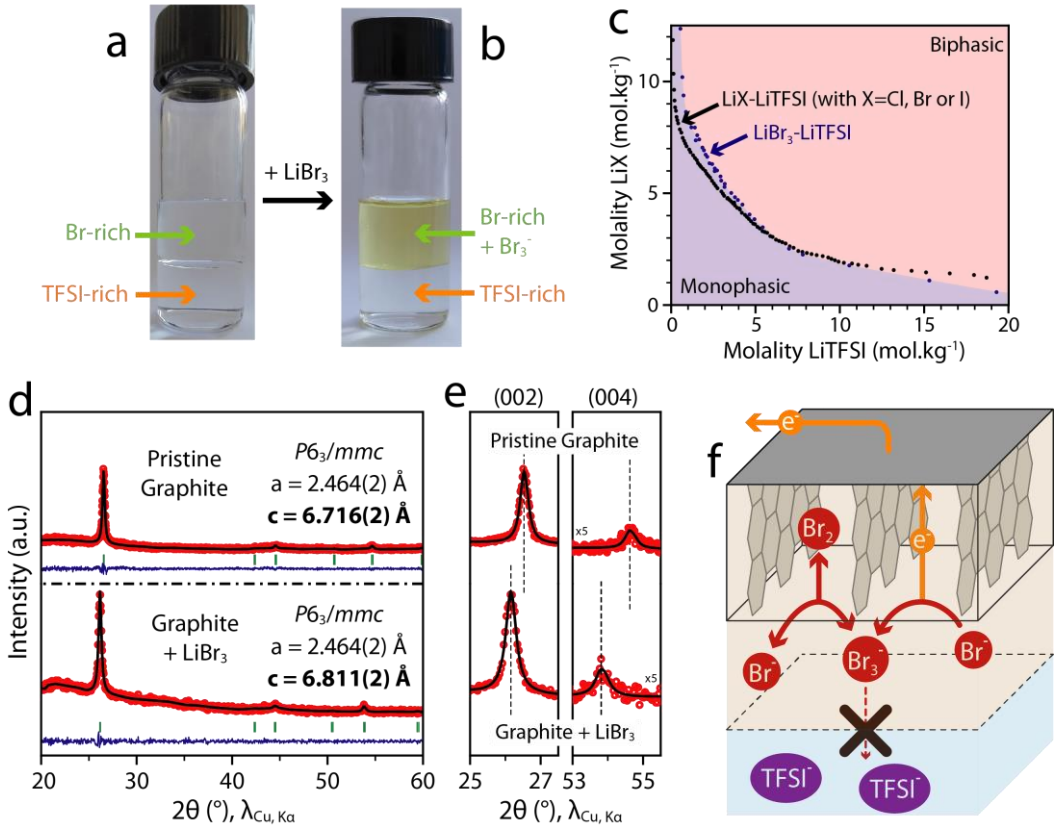

Figure 4. ABS confines Br_3^- in the Br-rich phase, enabling chemical intercalation of Br_2 into graphite. a-b, Pictures of the LiBr-LiTFSI system without (**a**) and with added $LiBr_3$ (**b**). **c**, Comparison of the phase diagram of the $LiBr_3$-LiTFSI system (dark blue) with the phase diagrams of the LiBr-LiTFSI system (black). **d-e**, Rietveld refinement (**d**) of the pristine graphite (top) and of graphite in contact with $LiBr_3$ (bottom). The red circles, black continuous line and bottom blue line represent the observed, calculated, and difference patterns respectively. Vertical green tick bars are the Bragg positions. A zoom on the (002) and (004) reflections is shown in (**e**). **f**, Scheme of the two-steps halides intercalation mechanism.

Thus far, our study revealed that at high concentration, halides are oxidized to trihalides at ≈0.85 V vs SHE for bromide (Fig. 2b and eq. 6) and at ≈1.25 V vs SHE for chloride (Fig. 2e and eq. 13), *i.e.* at potentials similar to those recorded for the conversion/intercalation of halogens into graphite (Fig. 1b). Such finding suggests that either trihalides are a side product of the conversion/intercalation reaction which is confined at the positive electrode in the halide-rich phase, the ABS thus avoiding cross-diffusion to the negative electrode and ensuring that trihalides can be reduced back during discharge, or that trihalides are involved into the conversion/intercalation mechanism. To probe if trihalides are involved into the conversion/intercalation mechanism, graphite electrodes were exposed to trihalide solutions, before to be analyzed by X-ray powder diffraction (Fig. 4d-e). A Rietveld refinement[30] confirms that pristine graphite presents an interlayer spacing of 6.716(2) Å, in line with previous reports[31] (Fig. 4d). However, when graphite is exposed to 10 m LiBr + 5 m $LiBr_3$, the (002) and (004) diffraction peaks shift to lower angles (Fig. 4e), indicating an interlayer spacing of graphite increase to 6.811(2) Å, as deduced from the Rietveld refinement (Fig. 4d). The increase of interlayer distance concurs with the intercalation of bromine into graphite, as previously reported[13,31], hence proving that trihalides are involved in the halogen intercalation mechanism following a chemical reaction (eq. 20):

$$X_3^- + C_6 = [C_6 - X_2] + X^- \quad (X = Br, Cl) \qquad eq.\ 20$$

Experimental results thus suggest that intercalation of halogen can follow a two-steps reaction, with first the electrochemical oxidation of halides to trihalides (eq. 3) followed by chemical intercalation of halogens into graphite (eq. 20). To assess the equilibrium between trihalides in solution and halogens intercalated in graphite, quantitative UV-Vis spectroscopy was conducted

after electrolysis of halide solutions using graphite electrodes (Fig. 5). Potentials of 0.9 V vs SHE and 1.3 V vs SHE are respectively measured for the electrolysis of 15m LiBr (Fig. 5a – red) and 15m LiCl (Fig. 5a – green) solutions (1.2 mA for 8 min, charged passed of 0.576 C), similar to the potentials of both halogens conversion/intercalation and halides oxidation to trihalides (Fig. 1 and Fig. 2b,e). UV-Vis conducted after the electrolysis of 15m LiBr shows the characteristic spectra of Br_3^- (Fig. 5b) while for the electrolysis of 15m LiCl, spectra is characteristic of $BrCl_2^-$ (Fig. 5c), most probably due to Br^- impurities coming from commercial LiCl salt (eq. S13). More importantly, theoretical concentrations calculated from the charge passed during the electrolysis ($Q_{electrolysis}$; Fig. 5a – blue) using Faraday law (Fig. 5d – blue) were then compared with absorption maximums (Fig. 5b-c) and experimental concentrations calculated using Beer-Lambert law (Fig. 5d – red and green). We found that the oxidation of halides to trihalides is predominant with efficiency calculated between 63% in 15m LiBr and 89% in 15m LiCl. Thus, our results demonstrate that the oxidation of halides to trihalides is not negligible and that part of the charged passed will be stored as trihalides in the electrolyte and not only as intercalated halogens in graphite.

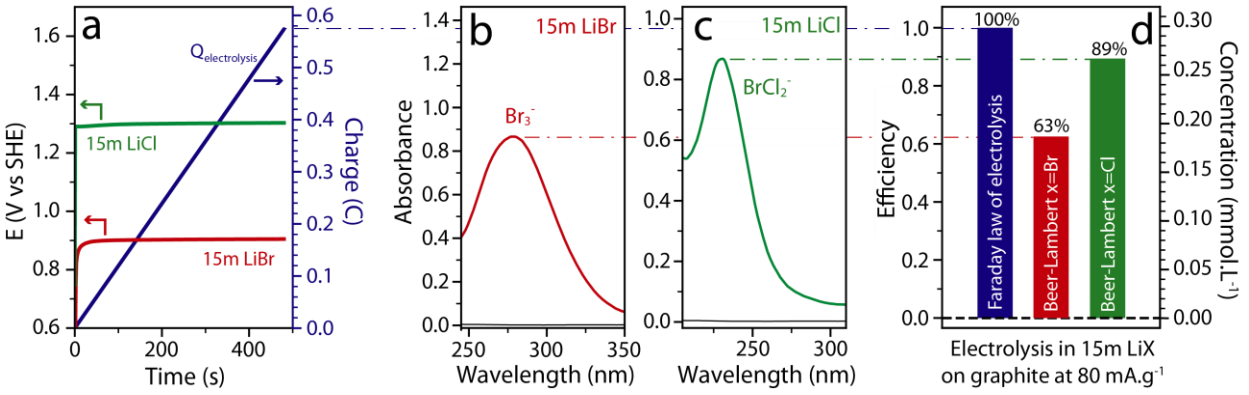

Figure 5. Electrolysis of LiBr and LiCl solutions along with quantitative UV-Vis to detect oxidation products. a, Chronopotentiometry at 1.2 mA for 8 minutes recorded for electrolysis of 15m LiBr (red) and

15m LiCl (green) solutions. In blue is plotted the charge passed during the electrolysis. **b-c**, UV-Vis spectra of the 15m LiBr (**b**) and 15m LiCl (**c**) electrolytes after electrolysis. **d**, Efficiency of the electrolysis calculated by comparing the ideal Faraday law of electrolysis with the concentration detected via Beer-Lambert law.

Overall, we proved that high concentrations of halide salts, as the ones find in ABS, enable the oxidation of halides to trihalides at potentials similar to the ones previously reported conversion/intercalation of halides into graphite. Moreover, the spontaneous intercalation of bromine into graphite via tribromide was proved to be possible. Hence, our electrochemical and spectroscopic results demonstrate that the intercalation of halogen into graphite can follow a two-steps intercalation with first the oxidation of halides to trihalides (eq. 3) followed by chemical intercalation of halogens (eq. 20). Such two-steps intercalation concurs with a recent study from Xu et al. using quasi-ionic liquid electrolyte[32] where halides are first oxidized to liquid halogens and then intercalated in graphite. An important implication of our finding is that trihalides in solution and the intercalated halogens (eq. 20) are in dynamic equilibrium, alike liquefied halogens with intercalated halogens[33]. Quantitative UV-Vis analysis proved that for the trihalides equilibrium, a none negligible part of the capacity is carried by trihalides in solution, as in a redox-flow catholyte, increasing the risk of self-discharge via the diffusion of trihalides to the negative electrode. However, our work unambiguously demonstrates that trihalides are poorly soluble in the TFSI-rich phase, *i.e.* the anolyte, demonstrating ABS to be the cornerstone in reaching good coulombic efficiencies by thermodynamically preventing the diffusion of trihalides to the negative electrode. Hence the development of ABS could be key to improve efficiencies of other dual-ion batteries such as zinc-halogen.[34–38] Moreover, by spontaneously separating the catholyte and anolyte without the use of expensive and fragile membranes, ABS show great

interest for a broad range of electrochemical devices, among which LiX-LiTFSI (with X=Cl, Br, I) ABS can be further used to develop membrane-less redox-flow batteries based on halides/trihalides redox. However, the use of ABS in electrochemical devices is still in its infancy, and further work is needed to improve our understanding of the electrochemistry of the ABS, especially concerning the selectivity and kinetics of ion transfer at liquid-liquid interface which will be critical for achieving both good coulombic efficiency and high power density.

Materials and Methods

Materials. Lithium bis(trifluoromethanesulfonyl)imide salt (LiTFSI Extra dry, Solvionic, 99.9%), lithium chloride salt (LiCl anhydrous, Alfa Aesar, 99%), lithium bromide salt (LiBr anhydrous, Alfa Aesar, 99%), Bromine liquid (Br_2, Sigma-Aldrich, 99%) were weighted and MilliQ water was added to reach the desired molalities. $LiBr_3$ solutions were obtained by adding equimolar quantities of Br_2 to LiBr solutions. Graphite (KS4, Imerys), activated carbon (YP-50F, Kuraray), Carbon black (Super P, Alfa Aesar) were used as received while Polytetrafluoroethylene (PTFE, Sigma-Aldrich, 60wt% dispersion in H_2O) was dried under vacuum overnight.

Batteries cycling. Self-standing electrodes were prepared in argon-filled glovebox (MBraun, O_2 < 0.1 ppm, H_2O < 0.1 ppm). Self-standing working electrodes (WE) were obtained by hand grinding LiBr/LiCL/KS4/SP with mass ratio of 2/1/6/3 before to be laminated with 10wt% of dried PTFE. Similarly, self-standing counter electrodes (CE) were obtained by laminating YP-50F with 10wt% of dried PTFE. Reference electrode (RE) was a leakless AgCl/Ag (ET069, eDAQ, 0.197 V vs SHE) regularly calibrated against RHE (HydroFlex, Gaskatel) in 1 $mol.L^{-1}$ H_2SO_4. Swagelok-type three-

electrode cells were assembled with the self-standing WE (6 mg) pressed on a titanium gauze (Ti, Alfa Aesar, 99.5%, 40 mesh, 0.127mm dia wire) separated from the self-standing CE and the RE by glass fibers sheets (GF/D, Whatmann) soaked in 20m LiTFSI before to be cycled on a potentiostat (VSP, Biologic) at 0.05 $mV.s^{-1}$.

Three-dimensional Pourbaix diagrams. The three-dimensional Pourbaix diagrams were obtained by plotting the lowest potential according to the following equations, applying the condition of concentration equality in element and assuming water activity to be unity (Supplementary discussion 1 and Fig. S8)[20]:

For bromide oxidation:

$$E = E°_{Br_2/Br^-} + \frac{RT}{2F} ln\left(\frac{c\left(Br_{2(aq)}\right)}{c\left(Br^-_{(aq)}\right)^2}\right) \text{ with } \frac{c\left(Br_{2(aq)}\right)}{c\left(Br^-_{(aq)}\right)} = \frac{1}{2} \text{ and } E°_{Br_2/Br^-} = 1.08 \text{ V vs SHE}$$

$$E = E°_{Br_3^-/Br^-} + \frac{RT}{2F} ln\left(\frac{c\left(Br_3^-_{(aq)}\right)}{c\left(Br^-_{(aq)}\right)^3}\right) \text{ with } \frac{c\left(Br_3^-_{(aq)}\right)}{c\left(Br^-_{(aq)}\right)} = \frac{1}{3} \text{ and } E°_{Br_3^-/Br^-} = 1.06 \text{ V vs SHE}$$

$$E = E°_{BrO_3^-/Br^-} + \frac{RT}{6F} ln\left(\frac{c\left(BrO_3^-_{(aq)}\right).a\left(H^+_{(aq)}\right)^6}{c\left(Br^-_{(aq)}\right).a\left(H_2O_{(l)}\right)^3}\right) \text{ with } \frac{c\left(BrO_3^-_{(aq)}\right)}{c\left(Br^-_{(aq)}\right)} = 1 \text{ and } E°_{BrO_3^-/Br^-} = 1.41 \text{ V vs SHE}$$

For chloride oxidation:

$$E = E°_{Cl_2/Cl^-} + \frac{RT}{2F} ln\left(\frac{c\left(Cl_{2(aq)}\right)}{c\left(Cl^-_{(aq)}\right)^2}\right) \text{ with } \frac{c\left(Cl_{2(aq)}\right)}{c\left(Cl^-_{(aq)}\right)} = \frac{1}{2} \text{ and } E°_{Cl_2/Cl^-} = 1.36 \text{ V vs SHE}$$

$$E = E°_{Cl_3^-/Cl^-} + \frac{RT}{2F} ln\left(\frac{c\left(Cl_3^-_{(aq)}\right)}{c\left(Cl^-_{(aq)}\right)^3}\right) \text{ with } \frac{c\left(Cl_3^-_{(aq)}\right)}{c\left(Cl^-_{(aq)}\right)} = \frac{1}{3} \text{ and } E°_{Cl_3^-/Cl^-} = 1.38 \text{ V vs SHE}$$

$$E = E°_{HClO/Cl^-} + \frac{RT}{2F} ln\left(\frac{c\left(HClO_{(aq)}\right).a\left(H^+_{(aq)}\right)}{c\left(Cl^-_{(aq)}\right).a\left(H_2O_{(l)}\right)}\right) \text{ with } \frac{c\left(HClO_{(aq)}\right)}{c\left(Cl^-_{(aq)}\right)} = 1 \text{ and } E°_{HClO/Cl^-} = 1.49 \text{ V vs SHE}$$

$$E = E°_{ClO^-/Cl^-} + \frac{RT}{2F} ln\left(\frac{c\left(ClO^-_{(aq)}\right).a\left(H^+_{(aq)}\right)^2}{c\left(Cl^-_{(aq)}\right).a\left(H_2O_{(l)}\right)}\right) \text{ with } \frac{c\left(ClO^-_{(aq)}\right)}{c\left(Cl^-_{(aq)}\right)} = 1 \text{ and } E°_{ClO^-/Cl^-} = 1.72 \text{ V vs SHE}$$

For iodide oxidation:

$$E = E°_{I_2/I^-} + \frac{RT}{2F} ln\left(\frac{c\left(I_{2(aq)}\right)}{c\left(I^-_{(aq)}\right)^2}\right) \text{ with } \frac{c\left(I_{2(aq)}\right)}{c\left(I^-_{(aq)}\right)} = \frac{1}{2} \text{ and } E°_{I_2/I^-} = 0.53 \text{ V vs SHE}$$

$$E = E°_{I_3^-/I^-} + \frac{RT}{2F} ln\left(\frac{a\left(I_3^-{}_{(aq)}\right)}{a\left(I^-_{(aq)}\right)^3}\right) \text{ with } \frac{c\left(I_3^-{}_{(aq)}\right)}{c\left(I^-_{(aq)}\right)^3} = \frac{1}{2} \text{ and } E°_{I_3^-/I^-} = 0.45 \text{ V vs SHE}$$

$$E = E°_{IO_3^-/I^-} + \frac{RT}{6F} ln\left(\frac{c\left(IO_3^-{}_{(aq)}\right).a\left(H^+_{(aq)}\right)^6}{c\left(I^-_{(aq)}\right).\, a\left(H_2O_{(l)}\right)^3}\right) \text{ with } \frac{c\left(IO_3^-{}_{(aq)}\right)}{c\left(I^-_{(aq)}\right)} = 1 \text{ and } E°_{IO_3^-/I^-} = 1.08 \text{ V vs SHE}$$

Halides oxidation on rotating disk electrode. Halides oxidation experiments were performed in three-electrode glass cell with about 10 mL of electrolyte degassed for 15 min with argon (Linde, HiQ 5.0). A saturated calomel electrode (SCE, OrigaLys, 0.242 V vs SHE) was used as RE, a flamed-annealed platinum gauze (Pt, Alfa Aesar, 99.9%, 100 mesh, 0.0762mm dia wire) in a fritted isolation compartment was used as CE, and a glassy carbon (GC, Pine Research, 0.196 cm^2_{geom}) on a rotating disk electrode setup (RDE, Pine Research, 1600rpm) as WE. Prior to any measurement, the GC electrode was sequentially polished with three slurries (6 µm diamond, 0.3 and 0.04 µm aluminum oxide, Presi) using a polishing machine (Le Cube, Presi) before to remove any residual traces of slurries by sonicating the electrodes three times in water/ethanol 50/50 (5 min each). All measurements were performed using a potentiostat (VSP, Biologic) and ohmic drop was measured after the electrochemical measurements via electrochemical impedance spectroscopy (EIS) and corrected manually during data treatment. Typical resistance between 5-15 Ω were measured.

Estimation of the potential shift due activity changes and the liquid junction potential (LJP). Open circuit voltage (OCV) at different molalities were measured with a potentiostat (VSP,

Biologic) in a two-electrode configuration between a SCE as RE and an ion selective electrode (ISE) to chloride (Cl-ISE) or bromide (Br-ISE), similarly to previously reported.[16] Halides ISE were prepared by oxidizing a silver wire (Ag, Alfa Aesar, 99.9%, 0.5mm dia) at constant current (i = 100 µA) for 1 hour in 1 mol.L^{-1} hydrobromic acid (HBr, Sigma-Aldrich, 48%, ACS reagent) for the Br-ISE, or in 1 mol.L^{-1} hydrochloric acid (HCl, Sigma-Aldrich, 30%, Suprapur) for the Cl-ISE using a three-electrode setup with a SCE as RE and a Pt gauze in a fritted isolation compartment as CE. Data analysis was performed according to the method previously describe (Degoulange et al.[16]) by calculating $\Delta E = \mathrm{OCV}(m) - \mathrm{OCV}(m_{Ref})$ and $\Delta E_N^c = \frac{RT}{2F} \ln\left(\frac{c_{halide}(m_{Ref})}{c_{\mathrm{halide}}(m)}\right)$ with m_{Ref} = 1m.

UV-Vis spectroscopy. UV-Vis spectra were recorded on a Mettler Toledo UV5bio spectrometer using an absorption quartz cell (Hellma analytics, Quartz Glass High Performance 200 nm – 2500 nm, 1mm optical path length). For UV-Vis spectra of Br_3^- and Br_2, Br_2 was added to a 15m LiBr or a 20m LiTFSI solution, respectively, making the background subtraction with respective solutions before addition of Br_2. From the spectra of the Br_2 saturated 20m LiTFSI solution, the solubility of Br_2 was estimated using Beer-Lambert law $A = \varepsilon.l.C$ with a molar extinction coefficient $\varepsilon_{420}(Br_2)$ = 165 mol^{-1}.L.cm^{-1} (Table S1). For UV-Vis spectra of Br_3^- in the Br-rich phase of the ABS, Br_2 was added to the ABS before to be vortexed for 1 min and then centrifuged at 6000rpm for 10 min, making the background subtraction from the centrifuged ABS before Br_2 addition. Centrifugation was key to properly separate the ABS and thus to limit Rayleigh scattering from emulsion of the ABS phases.

ABS phase diagram. Phase diagrams were measured using the cloud point titration method previously described.[9–11] Briefly, starting from a known mass of a concentrated solution of one

component ($LiBr_3$ or LiTFSI), a concentrated solution of the second component is weighed while being added dropwise and vortexed until the solution turns cloudy. Then, MilliQ water is weighed while being added dropwise and vortexed until the solution turns clear again (even though still showing the red color). These steps are repeated for each point of the diagram.

XRD diffraction and Rietveld refinement. Powder X-ray diffraction (XRD) patterns were taken in Bragg−Brentano geometry (Bruker D8 Advance, Cu Kα X-ray source, λ_1 = 1.5406 Å, λ_2 = 1.5444 Å, LYNXEYE XE detector). Graphite was put in contact with 10m LiBr + 5m $LiBr_3$ in a sealed capillary (Capillary Tube Supplies Ltd, borosilicate glass, 0.6 mm outside dia, 0.01 mm wall thickness) while pristine graphite was put alone in the sealed capillary. Both diffraction patterns were refined using the FullProf program.[30]

Quantitative electrolysis. Electrolysis measurements were performed in three-electrode glass cell with 10 mL of electrolyte degassed for 15 min with Ar. A SCE was used as RE, a flamed-annealed Pt gauze in a fritted isolation compartment was used as CE and self-standing obtained by laminating KS4 with 10wt% of dried PTFE before to be pressed on a Ti gauze used as WE. Electrolysis was performed (VSP, Biologic) at constant current of i = 1.2 mA (equivalent to 200 $mA.g^{-1}_{ks4}$ with 6mg KS4 and equivalent to 80 $mA.g^{-1}_{LBC\text{-}G}$ as reported by Yang et al.[13]) for t = 8 min leading to a charge $Q_{electrolysis} = i.\Delta t$ equivalent to a concentration through the faraday law of electrolysis $C_{Faraday} = \frac{Q_{electrolysis}}{n.F.V}$ with n = 2 and V = 10 mL. This concentration is compared to the concentration estimated using Beer-Lambert law with $\varepsilon_{272}(Br_3^-)$ = 46600 $mol^{-1}.L.cm^{-1}$ for the electrolysis of 15m LiBr and $\varepsilon_{232}(BrCl_2^-)$ = 32700 $mol^{-1}.L.cm^{-1}$ for the electrolysis of 15m LiCl (Table S1).

Supporting Information

See the supporting information for additional equations, discussion, tables and data regarding halides oxidation and UV-Vis absorption.

Notes

The authors declare no conflict of interest.

Acknowledgments

The authors acknowledge the French National Research Agency for its support through the Labex STORE-EX project (ANR-10LABX-76-01) and through the projects BALWISE (ANR-19-CE05-0014). The authors thanks Jean-Marie Tarascon (College de France, Paris, France) for useful discussions.

References

1. Deng, H. & Aifantis, K. E. Applications of Lithium Batteries. in *Rechargeable Ion Batteries* 83–103 (John Wiley & Sons, Ltd, 2023). doi:10.1002/9783527836703.ch4.
2. Net Zero by 2050 – Analysis. *IEA* https://www.iea.org/reports/net-zero-by-2050.
3. Zhu, Z. *et al.* Rechargeable Batteries for Grid Scale Energy Storage. *Chem. Rev.* **122**, 16610–16751 (2022).
4. Grey, C. P. & Tarascon, J. M. Sustainability and in situ monitoring in battery development. *Nature Mater* **16**, 45–56 (2017).
5. Borodin, O., Self, J., Persson, K. A., Wang, C. & Xu, K. Uncharted Waters: Super-Concentrated Electrolytes. *Joule* **4**, 69–100 (2020).
6. Suo, L. *et al.* "Water-in-salt" electrolyte enables high-voltage aqueous lithium-ion chemistries. *Science* **350**, 938–943 (2015).

7. Yamada, Y. *et al.* Hydrate-melt electrolytes for high-energy-density aqueous batteries. *Nature Energy* **1,** 1–9 (2016).
8. Kühnel, R.-S., Reber, D. & Battaglia, C. Perspective—Electrochemical Stability of Water-in-Salt Electrolytes. *J. Electrochem. Soc.* **167,** 070544 (2020).
9. Dubouis, N. *et al.* Chasing Aqueous Biphasic Systems from Simple Salts by Exploring the LiTFSI/LiCl/H2O Phase Diagram. *ACS Cent. Sci.* **5,** 640–643 (2019).
10. Dubouis, N., France-Lanord, A., Brige, A., Salanne, M. & Grimaud, A. Anion Specific Effects Drive the Formation of Li-Salt Based Aqueous Biphasic Systems. *J. Phys. Chem. B* **125,** 5365–5372 (2021).
11. Degoulange, D. *et al.* Direct imaging of micrometer-thick interfaces in salt–salt aqueous biphasic systems. *Proceedings of the National Academy of Sciences* **120,** e2220662120 (2023).
12. Yang, C. *et al.* Unique aqueous Li-ion/sulfur chemistry with high energy density and reversibility. *PNAS* **114,** 6197–6202 (2017).
13. Yang, C. *et al.* Aqueous Li-ion battery enabled by halogen conversion–intercalation chemistry in graphite. *Nature* **569,** 245–250 (2019).
14. Navalpotro, P. *et al.* Pioneering Use of Ionic Liquid-Based Aqueous Biphasic Systems as Membrane-Free Batteries. *Advanced Science* **5,** 1800576 (2018).
15. Navalpotro, P., Ibañez, S. E., Pedraza, E. & Marcilla, R. A neutral pH aqueous biphasic system applied to both static and flow membrane-free battery. *Energy Storage Materials* **56,** 403–411 (2023).
16. Degoulange, D., Dubouis, N. & Grimaud, A. Toward the understanding of water-in-salt electrolytes: Individual ion activities and liquid junction potentials in highly concentrated aqueous solutions. *J. Chem. Phys.* **155,** 064701 (2021).

17. Chen, H., Kaliyaraj Selva Kumar, A., Le, H. & Compton, R. G. Non-unity stoichiometric reversible electrode reactions. The effect of coupled kinetics and the oxidation of bromide. *Journal of Electroanalytical Chemistry* **876**, 114730 (2020).
18. Vos, J. G., Venugopal, A., Smith, W. A. & Koper, M. T. M. Competition and Interhalogen Formation During Parallel Electrocatalytic Oxidation of Bromide and Chloride on Pt. *J. Electrochem. Soc.* **167**, 046505 (2020).
19. Vos, J. G., Venugopal, A., Smith, W. A. & Koper, M. T. M. Competition and selectivity during parallel evolution of bromine, chlorine and oxygen on IrOx electrodes. *Journal of Catalysis* **389**, 99–110 (2020).
20. Robinson, R. A. The water activities of lithium chloride solutions up to high concentrations at 25°. *Trans. Faraday Soc.* **41**, 756–758 (1945).
21. Thermodynamics of Cl-H2O, Br-H2O, I-H2O, Au-Cl-H2O, Au-Br-H2O and Au-I-H2O systems at 298 K. *Journal of Electroanalytical Chemistry* **361**, 13–24 (1993).
22. Han, K. S. *et al.* Origin of Unusual Acidity and Li+ Diffusivity in a Series of Water-in-Salt Electrolytes. *J. Phys. Chem. B* **124**, 5284–5291 (2020).
23. Bard, A. J. & Faulkner, L. R. *Electrochemical Methods: Fundamentals and Applications, 2nd Edition*. (2000).
24. Lide, D. R. *et al.* CRC Handbook of Chemistry and Physics. (2005).
25. Awtrey, A. D. & Connick, R. E. The Absorption Spectra of I_2, I_3^-, I^-, IO_3^-, $S_4O_6^=$ and $S_2O_3^=$. Heat of the Reaction $I_3^- = I_2 + I^-$. *J. Am. Chem. Soc.* **73**, 1842–1843 (1951).
26. Popov, A. I. & Swensen, R. F. Studies on the Chemistry of Halogens and of Polyhalides. V. Spectrophotometric Study of Polyhalogen Complexes in Acetonitrile and in Ethylene Dichloride. *J. Am. Chem. Soc.* **77**, 3724–3726 (1955).

27. Seery, D. J. & Britton, D. The Continuous Absorption Spectra of Chlorine, Bromine, Bromine Chloride, Iodine Chloride, and Iodine Bromide. *J. Phys. Chem.* **68**, 2263–2266 (1964).
28. Gabes, W. & Stufkens, D. J. Electronic absorption spectra of symmetrical and asymmetrical trihalide ions. *Spectrochimica Acta Part A: Molecular Spectroscopy* **30**, 1835–1841 (1974).
29. Wang, T. X., Kelley, M. D., Cooper, J. N., Beckwith, R. C. & Margerum, D. W. Equilibrium, Kinetic, and UV-Spectral Characteristics of Aqueous Bromine Chloride, Bromine, and Chlorine Species. *Inorg. Chem.* **33**, 5872–5878 (1994).
30. Rodríguez-Carvajal, J. Recent advances in magnetic structure determination by neutron powder diffraction. *Physica B: Condensed Matter* **192**, 55–69 (1993).
31. Sasa, T., Takahashi, Y. & Mukaibo, T. Crystal structure of graphite bromine lamellar compounds. *Carbon* **9**, 407–416 (1971).
32. Xu, J. *et al.* Lithium halide cathodes for Li metal batteries. *Joule* **7**, 83–94 (2023).
33. Dresselhaus, M. S. & Dresselhaus, G. Intercalation compounds of graphite. *Advances in Physics* **51**, 1–186 (2002).
34. Liu, H. *et al.* A Zinc–Dual-Halogen Battery with a Molten Hydrate Electrolyte. *Advanced Materials* **32**, 2004553 (2020).
35. Ejigu, A., Le Fevre, L. W. & Dryfe, R. A. W. Reversible Electrochemical Energy Storage Based on Zinc-Halide Chemistry. *ACS Applied Materials and Interfaces* **13**, 14112–14121 (2021).
36. Zou, Y. *et al.* A four-electron Zn-I 2 aqueous battery enabled by reversible I − /I 2 /I + conversion. *Nature Communications* **12**, 170 (2021).
37. Cai, S. *et al.* Water–Salt Oligomers Enable Supersoluble Electrolytes for High-Performance Aqueous Batteries. *Advanced Materials* **33**, 2007470 (2021).
38. Guo, Q. *et al.* Reversible Insertion of I–Cl Interhalogen in a Graphite Cathode for Aqueous Dual-Ion Batteries. *ACS Energy Lett.* 459–467 (2021) doi:10.1021/acsenergylett.0c02575.